NeuroImage 59 (2012) 3941–3954

Contents lists available at SciVerse ScienceDirect

NeuroImage

journal homepage: www.elsevier.com/locate/ynimg

Structure Tensor Informed Fiber Tractography (STIFT) by combining gradient echo MRI and diffusion weighted imaging

Michiel Kleinnijenhuis [a,b,*], Markus Barth [a,c], Daniel C. Alexander [d], Anne-Marie van Cappellen van Walsum [b,e], David G. Norris [a,c,e]

[a] Radboud University Nijmegen, Donders Institute for Brain, Cognition and Behaviour, Kapittelweg 29, 6525 EN, Nijmegen, Netherlands
[b] Department of Anatomy, Radboud University Nijmegen Medical Centre, Huispost 109 Anatomie, Postbus 9101, 6500 HB, Nijmegen, Netherlands
[c] Erwin L. Hahn Institute for Magnetic Resonance Imaging, UNESCO World Cultural Heritage Zollverein, Arendahls Wiese 199, D-45141, Essen, Germany
[d] Centre for Medical Image Computing, Department of Computer Science, University College London, Gower Street, London WC1E 6BT, UK
[e] MIRA Institute for Biomedical Technology and Technical Medicine, University of Twente, Postbus 217, 7500 AE, Enschede, Netherlands

ARTICLE INFO

Article history:
Received 18 April 2011
Revised 30 September 2011
Accepted 20 October 2011
Available online 28 October 2011

Keywords:
Tractography
Structure tensor
Gradient echo imaging
Diffusion weighted imaging
Optic radiation
Cingulum

ABSTRACT

Structural connectivity research in the human brain *in vivo* relies heavily on fiber tractography in diffusion-weighted MRI (DWI). The accurate mapping of white matter pathways would gain from images with a higher resolution than the typical ~2 mm isotropic DWI voxel size. Recently, high field gradient echo MRI (GE) has attracted considerable attention for its detailed anatomical contrast even within the white and gray matter. Susceptibility differences between various fiber bundles give a contrast that might provide a useful representation of white matter architecture complementary to that offered by DWI.

In this paper, Structure Tensor Informed Fiber Tractography (STIFT) is proposed as a method to combine DWI and GE. A data-adaptive structure tensor is calculated from the GE image to describe the morphology of fiber bundles. The structure tensor is incorporated in a tractography algorithm to modify the DWI-based tracking direction according to the contrast in the GE image.

This GE structure tensor was shown to be informative for tractography. From closely spaced seedpoints (0.5 mm) on both sides of the border of 1) the optic radiation and inferior longitudinal fasciculus 2) the cingulum and corpus callosum, STIFT fiber bundles were clearly separated in white matter and terminated in the anatomically correct areas. Reconstruction of the optic radiation with STIFT showed a larger anterior extent of Meyer's loop compared to a standard tractography alternative. STIFT in multifiber voxels yielded a reduction in crossing-over of streamlines from the cingulum to the adjacent corpus callosum, while tracking through the fiber crossings of the centrum semiovale was unaffected.

The STIFT method improves the anatomical accuracy of tractography of various fiber tracts, such as the optic radiation and cingulum. Furthermore, it has been demonstrated that STIFT can differentiate between kissing and crossing fiber configurations. Future investigations are required to establish the applicability in more white matter pathways.

Introduction

As a method for mapping white matter (WM) pathways in the human brain *in vivo*, fiber tractography (Conturo et al., 1999; Jones et al., 1999; Mori et al., 1999) has provided invaluable insights into the structural connections between brain regions. Fiber tracking is based on the anisotropy of water diffusion profiles (Basser et al., 1994) measured by Diffusion Weighted Imaging (DWI). This anisotropy arises from restriction of water diffusion by tissue microstructure, particularly the axonal membranes and myelin sheets in the white matter (Beaulieu, 2002).

Although fiber tracking has proven to be vital to cognitive neuroscience, with its typical >8 ml voxels DWI offers a rather coarse description of the microanatomical substrate that tractography attempts to reconstruct. Consequently, many voxels contain a mixture of white and gray matter, or multiple tracts and fiber orientations. How to deal with these multifiber voxels is one of the major challenges in tractography. The same complex diffusion profile can represent various fiber configurations, e.g. crossing or kissing tracts and fanning or splitting tracts (Seunarine and Alexander, 2009), leading

Abbreviations: STIFT, Structure Tensor Informed Fiber Tractography; DWI, diffusion weighted imaging; GE, gradient echo; WM, white matter; GM, gray matter; CSF, cerebrospinal fluid; OR, optic radiation; ILF, inferior longitudinal fasciculus; IFOF, inferior fronto-occipital fasciculus; (d)LGN, (dorsal) lateral geniculate nucleus; CC, corpus callosum; CG, cingulum; CS, centrum semiovale; CST, corticospinal tract.

* Corresponding author at: Radboud University Nijmegen Medical Centre, Department of Anatomy, Huispost 109 Anatomie, Postbus 9101, 6500 HB Nijmegen, The Netherlands. Fax: +31 24 36 13789.
E-mail addresses: M.Kleinnijenhuis@anat.umcn.nl (M. Kleinnijenhuis), markus.barth@donders.ru.nl (M. Barth), D.Alexander@cs.ucl.ac.uk (D.C. Alexander), A.vanCappellenvanWalsum@anat.umcn.nl (A.-M. van Cappellen van Walsum), david.norris@donders.ru.nl (D.G. Norris).

1053-8119/$ – see front matter © 2011 Elsevier Inc. All rights reserved.
doi:10.1016/j.neuroimage.2011.10.078

to ambiguity in the reconstruction of fiber pathways. The limited spatial resolution and the associated partial volume effects largely determine the degree to which fiber tracts can be accurately resolved by tractography. The considerable benefits of small voxel sizes for resolving fiber tracking ambiguity have been demonstrated in animal (Dyrby et al., 2007; Wedeen et al., 2008) and human (McNab et al., 2009; Roebroeck et al., 2008) *ex vivo* investigations. However, for connectivity research in the human brain *in vivo* sensitivity demands have hitherto made it difficult to attain voxels smaller than ~2×2×2 mm. Initial reports utilizing smaller voxel sizes (Heidemann et al., 2010; McNab et al., 2010) look promising, but have yet to be extended to whole-brain investigations acquired in a reasonable amount of time. Track density imaging (Calamante et al., 2010) provides a post-processing approach to increase effective resolution, but relies on the accuracy of fiber tracking in low-resolution DWI.

In recent years, it has been shown that gradient echo MRI (GE) can provide clues about white matter architecture at *submillimeter* resolution, albeit not with the directional information offered by DWI. The T_2*-weighted GE magnitude and phase reflect variations in the distribution of para- and diamagnetic substances that cause differences in susceptibility between tissue types. This effect has mainly been utilized for MR BOLD venography where paramagnetic deoxyhemoglobin causes a large dephasing in veins as compared to the surrounding tissue (Ogawa et al., 1990; Reichenbach et al., 1997).

At high field strength, major fiber bundles such as the optic radiations (OR), cinguli (CG), and corpus callosum (CC) can be identified, with high contrast to surrounding fiber bundles (Li et al., 2006). The mechanisms underlying these WM susceptibility effects in GE imaging are a topic of active investigation. Several candidate mechanisms, such as bulk susceptibility effects and orientation of the fiber bundle with respect to the main magnetic field have been proposed and investigated for their relative contribution in the various tissue types (see Duyn, 2010 for a review).

Concentrations of susceptibility inclusions (chemical elements that alter the tissue's susceptibility) can account for a large portion of the spatial R_2* variations in WM. Similar to the effect of deoxyhemoglobin in veins, paramagnetic ferritin-bound brain iron has been shown to play a major role in the GE contrast between cortical layers (Fukunaga et al., 2010) and for subcortical structures (Langkammer et al., 2010). In white matter, however, iron content appears not to be the dominant factor (Langkammer et al., 2010; Li et al., 2009). *Myelination* of the fiber bundles has been indicated as the main source of R_2* contrast in white matter at high field (Li et al., 2009). Due to the protein-induced frequency shifts myelin is lightly diamagnetic, thus differences in myelin composition, cellular architecture and myelination density between fiber bundles can give rise to R_2* contrast (Duyn, 2010).

Notwithstanding the importance of concentrations of susceptibility inclusions, they are not the only determinant of R_2* values. Especially in white matter, the orientation of the tissue with respect to the main magnetic field modulates R_2* (Schäfer et al., 2009; Wiggins et al., 2008). This effect is thought to arise from the highly ordered parallel cylindrical structure of the lipid bilayer of the myelin sheets. Moreover, the anisotropic organization of the cellular structure (e.g. myelin) is reflected in tissue susceptibility (Lee et al., 2011) and phase (He and Yablonskiy, 2009). The R_2* orientation dependence has been characterized and validated in several recent experiments comparing GE and DWI (Bender and Klose, 2010; Cherubini et al., 2009; Denk et al., 2011; Lee et al., 2011), showing R_2* modulations of more than 6 Hz between the parallel and perpendicular orientation to the main magnetic field (Lee et al., 2011).

Considering the difficulties associated with the low resolution of DWI on the one hand and the sensitivity of the high resolution GE image to white matter architecture on the other hand, we hypothesize that fiber tracking can be improved by incorporating information obtained from the GE image in tractography algorithms. The imaging modalities should be combined in such a way as to exploit their respective advantages: high *angular* resolution in DWI and high *spatial* resolution in GE. The combination might thus allow a more accurate description of white matter anatomy than is achieved with current tractography methods.

Several tracts show R_2* contrast and are therefore candidates to test our hypothesis. Each can illustrate various aspects of the tractography outcome, such as tract morphology, connectivity fingerprint and multifiber behavior. In this initial demonstration, we seed fibers in two WM regions: the occipitotemporal and frontoparietal WM. Within the occipitotemporal WM, the optic radiation is a tract of particular interest, because 1) it is a very prominent WM structure in the GE image, 2) it has unambiguous anatomical source and target, i.e. it connects the lateral geniculate nucleus in the thalamus with the primary visual cortex (V1) in the calcarine sulcus (Nieuwenhuys et al., 2008); and 3) it features Meyer's loop, an area that is problematic for tractography (Thiebaut de Schotten et al., 2011). Accurate tractography of Meyer's loop has important clinical relevance for presurgical planning, because visual field defects can occur if part of this temporal loop of the OR is resected (van Baarsen et al., 2009).

In the frontoparietal WM, we focus on the cingulum, corticospinal tract (CST) and corpus callosum. On its lateral border, the cingulum is adjacent to the body of the corpus callosum. As a result, the DWI has many voxels containing two fiber populations: CG fibers running in the sagittal plane and CC fibers in the coronal plane. Due to their different R_2* values (Cherubini et al., 2009), this border between the CG and CC is also observed in the GE magnitude. The GE image might be informative to disentangle these fiber bundles in tractography. The frontoparietal WM also contains a region that is regarded as one of the most dense fiber crossings in the brain. The centrum semiovale (CS) contains fibers from the corpus callosum, corona radiata and arcuate fasciculus that weave their fibers through this region in the mediolateral, dorsoventral and rostrocaudal directions, respectively. Consequently, the medial frontoparietal WM is an area well suited to assess the potential for the combination of DWI and GE in the presence of multiple fiber populations within a voxel.

In the present work, we exploit the additional information that can be obtained from high-resolution scalar images—GE magnitude in particular—to inform DWI tractography algorithms. The specific method we put forward is Structure Tensor Informed Fiber Tractography (STIFT).

Methods

MR data acquisition

Images were acquired in two healthy male volunteers after they gave informed consent according to the protocols approved by the Institutional Review Boards of the two sites involved. Diffusion weighted and T1-weighted scans were performed on a 3 T Siemens Magnetom Trio system (Siemens, Erlangen, Germany) using a 32-channel array head coil at the Donders Institute of the Radboud University Nijmegen. Gradient echo images were acquired on a 7 T system (Siemens, Erlangen, Germany) at the Erwin L. Hahn Institute in Essen. Different main magnetic field strengths were used to ensure optimal quality of the DWI and optimal contrast within white matter using GE.

The DWI data were recorded using a twice-refocused spin-echo EPI sequence (TR/TE = 8300/95 ms; AF = 2) with a matrix size of 110×110 and a field of view (FOV) of 220×220 mm. Sixty-four contiguous 2.0 mm slices were acquired in oblique orientation resulting in whole-brain coverage with 2.0 mm isotropic voxels. Diffusion weightings with a b-value of 1000 s/mm^2 were applied in 61 directions according to the scheme proposed by Cook et al. (2007), interleaved with seven volumes without diffusion weighting (TA = 9 minutes). For T1-weighted images an MPRAGE sequence (TR/TE/TI = 2300/3/1100 ms; AF = 2) was used. Whole-head images were obtained by

acquiring 192 slices of 1.0 mm thickness with a matrix size of 256×256 and FOV of 256×256 mm (TA = 6 min). GE images were recorded at 7 T in supine headfirst position using a fully first order flow-compensated 3D FLASH sequence (TR/TE = 36/23 ms; flip angle = 15°; BW 120 Hz/px) with an isotropic resolution of 0.5 mm. For subject 1, GE images were acquired using an 8-ch head coil with subject-specific geometrical parameters: matrix size = 448×336; FOV = 224×168 mm; 208 slices; AF = 2; TA = 23 min. For subject 2, a 32-ch coil was available and the parameters were: matrix size = 448×448; FOV = 224×224 mm; 224 slices; AF = 3; TA = 16 min.

Data processing

Preprocessing

A schematic overview of STIFT data processing is provided in Fig. 1. The FreeSurfer v4.0.5 (Dale et al., 1999; Fischl et al., 1999) analysis pipeline (http://surfer.nmr.mgh.harvard.edu/fswiki/RecommendedReconstruction) was applied to the T1-weighted data sets to obtain a brain-extracted and intensity-normalized T1-weighted volume, as well as subcortical segmentations and cortical parcellations. For the GE image, brain extraction and bias field correction were performed using FSL v4.1.5 (Smith et al., 2004).

Because accurate alignment of WM structures between images is crucial for this method, special care was taken in this processing step. The T1 and GE images were coregistered in a two-step procedure using the normalized mutual information algorithm with 6 degrees of freedom implemented in FSL v4.1.5. In the first step, weighting volumes were used to disregard the temporal lobes where the GE image was inhomogeneous due to the slab profile (WV1). In a second step, the GE-to-T1 coregistration was fine-tuned by using a weighting volume obtained by dilating the FreeSurfer segmentation of the cortical ribbon by one voxel (WV2). Using this weighting, the images are coregistered on the gray-white matter surfaces of the cortical ribbon evident in both T1 and GE images, while masking the many structures causing large intensity variations that are present in the GE image but not in the T1 image (e.g. basal ganglia, optic radiations and large veins).

Diffusion weighted images were preprocessed with the SPM-based PATCH toolbox (Zwiers, 2010). This toolbox was used to perform automated motion and cardiac artifact correction, image realignment, coregistration and unwarping to the T1 image. The unwarping of the DWI volumes was performed by means of an algorithm constrained to the phase encoding direction (Visser et al., 2010) that warps the mean of the realigned non-diffusion weighted images to the T1 image (Supplementary material: Animation S1). The purpose of the unwarping was to reduce EPI distortion in the (anterior–posterior) phase-encoding direction, thus optimizing the T1-to-DWI and, consequently, GE-to-DWI coregistration (Supplementary material: Animation S2).

Structure tensor

To directly and meaningfully incorporate the information in the scalar GE image in tractography algorithms, a structure tensor is calculated. A structure tensor describes features in the image by considering a local neighborhood. This description allows for image analysis applications such as edge and corner detection, orientation and texture analysis and optic flow estimation (Brox et al., 2006). Orientation of elements in an image, for instance, can be estimated from the local vector field of intensity gradients. The outer product of the gradient vector, which is a 3×3 structure tensor, is used to avoid cancelation effects for elements that are thinner than the neighborhood. By integrating data in

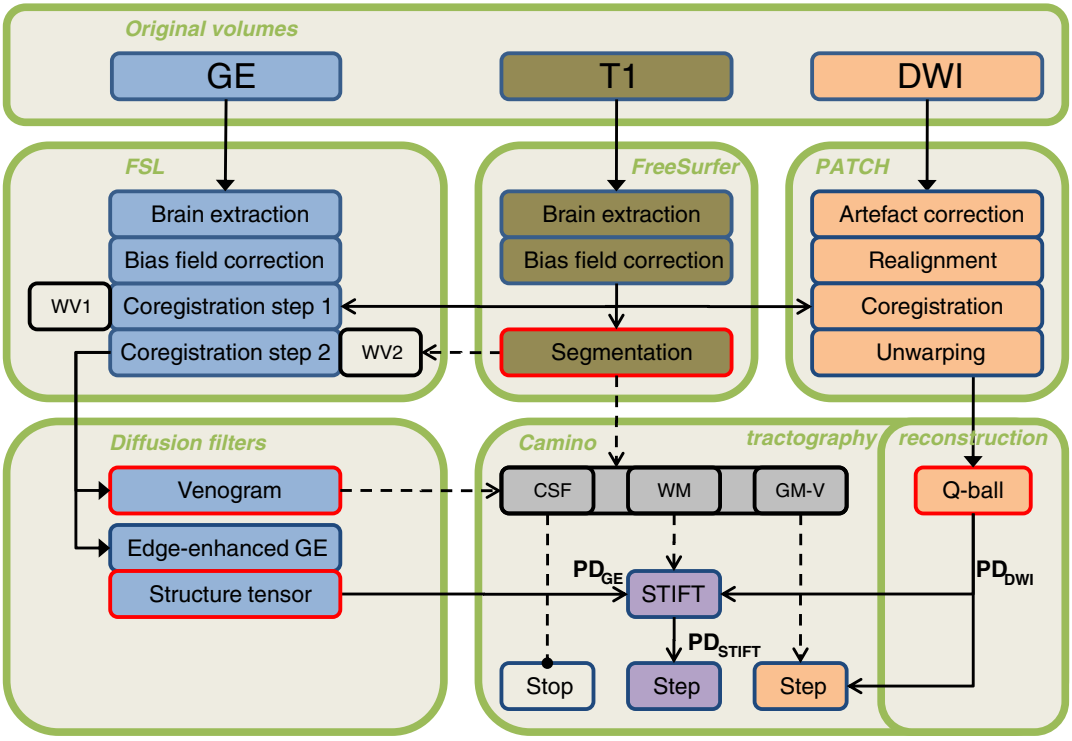

Fig. 1. STIFT processing pipeline. The brain is extracted from the GE image and bias field correction is performed in FSL (upper left). Similar steps are performed in the FreeSurfer pipeline for the T1-weighted image. Furthermore, a white-gray matter segmentation results from the FreeSurfer analysis (upper middle). The GE image is coregistered (but not resliced) to the intensity-normalized T1 volume masking the base of the brain where the GE showed a slab profile with a weighting volume (WV1) and then using a FreeSurfer-based weighting volume of the cortical ribbon (WV2). A venogram and edge-enhanced GE image are then calculated from the GE image (lower left). The structure tensor field is calculated from the edge-enhanced GE image. In the DWI flow chart (upper right), PATCH is used to correct artifacts, perform realignment, coregistration to the T1 volume and unwarping of EPI distortions to the T1 volume. Camino is used to reconstruct Q-ball orientation density functions and detect the peaks. For tractography (lower right), the current tracking point is interpolated in the venogram and T1-segmentation and classified as CSF, WM, GM or Vein (V). The Q-ball peak direction PD_{DWI} and structure tensor peak direction PD_{GE} are also interpolated from the vector fields at the current point. Tracking proceeds with one of three options, depending on the classification. Either 1) tracking is terminated (in CSF); 2) a step is taken in direction PD_{DWI} (in GM or V); or 3) the STIFT adaptation is calculated from PD_{DWI} and PD_{GE} after which a step is taken in direction PD_{STIFT} (in WM).

the neighborhood of a point (smoothing) the orientation estimation is robust in the presence of noise in the image (Brox et al., 2006).

Most of the white matter fiber bundles observed in the GE image have a sheet-like geometry. The features of interest for the presently proposed STIFT algorithm are the borders between fiber sheets. These take the shape of curved planes. The local orientation estimation of these planes is affected by inhomogeneities in the GE image. In particular, small veins penetrating the fiber bundles, but also image noise, are a nuisance. For a robust estimation of the local orientation of the WM border planes, a data-adaptive structure tensor was used. The neighborhood over which the structure tensor is integrated can be designed to enhance planar edges (Weickert, 1998). For this structure tensor, smoothing occurs preferentially in the direction of fiber bundles, while limiting smoothing over the edges between fiber bundles. In the present work we used a nonlinear anisotropic diffusion filter from Kroon and Slump (2009) (http://www.mathworks.com/matlabcentral/fileexchange/25449-image-edge-enhancing-coherence-filter-toolbox) to calculate an edge-enhanced GE image and structure tensor (Appendix A).

Structure Tensor Informed Fiber Tractography (STIFT)

STIFT algorithm

Tractography algorithms implemented in the Camino toolkit v2.873 (Cook et al., 2006) were adapted to incorporate the structure tensor by directly influencing the tracking direction (see Supplementary material: Animation S3). The adapted tracking direction PD_{STIFT} is calculated as follows: the original tracking direction PD_{DWI} is rotated towards the plane orthogonal to the first eigenvector of the structure tensor PD_{GE} and proportional to its first eigenvalue $\lambda_{PD_{GE}}$:

$$PD_{STIFT} = \lambda_w \cdot \widehat{P}_{\perp} + (1-\lambda_w) \cdot PD_{DWI} \quad (1)$$

where

$$P_{\perp} = PD_{GE} \times (PD_{DWI} \times PD_{GE})$$

and

$$\begin{array}{ll} \lambda_w = 1 & \\ \lambda_w = \lambda_{PD_{GE}}/W & \text{for} \quad \begin{array}{l} \lambda_{PD_{GE}} > W \\ \lambda_{PD_{GE}} \leq W \end{array} \end{array}.$$

W is the free parameter that determines the structure tensor weighting. In the present study, W was chosen equal to the first eigenvalue of structure tensor on the outer border of the optic radiation.

Because the structure tensor is also prominent for edges in the GE image not reflecting white matter contrasts (such as veins and the gray-white matter border), the STIFT adaptation of the tracking direction was used only in white matter voxels. The FreeSurfer segmentation results of white matter, gray matter and CSF (cerebrospinal fluid) were used as masks. Additionally, a venogram was created from the GE image using a vessel enhancing diffusion (VED) filter optimized to detect large veins (Koopmans et al., 2008). The smaller veins were effectively smoothed by the edge-enhancing diffusion filter. The venogram was thresholded to select large veins and binarized. The venogram and the binary cortex mask were dilated using mean dilation with a $3\times3\times3$ box kernel to include the gradient on the white-matter side of the tissue borders. In every tracking step, the current point was classified as belonging to white matter, gray matter, CSF or a vein. In white matter the STIFT method was used; in gray matter and veins the original tracking direction was used; and tracking was terminated when the point was classified as CSF.

Seeds and tractography

Two approaches were taken to investigate tracking behavior of the STIFT method. First, seed point pairs were placed in the centers of neighboring GE voxels within and on the border of neighboring tracts, because it can be expected that the effect of STIFT is largest at tract borders. STIFT was evaluated by this approach for two different WM areas: 1) the occipitotemporal area, seeding in the optic radiation and inferior longitudinal fasciculus/inferior fronto-occipital fasciculus (ILF/IFOF) fiber complex; 2) the medial frontoparietal area, seeding in the cingulum and corpus callosum. Additionally, three seed point pairs were placed in the centrum semiovale. Second, seed regions were drawn lateral to the lateral geniculate nucleus (LGN) to track the fibers of the optic radiation. The (dilated) cortical parcellations of the left and right pericalcarine cortices from the FreeSurfer analysis were used as waypoints. Tracts were truncated upon first entry of the waypoint.

In Camino, Q-ball orientation density functions (Descoteaux et al., 2007; Tuch, 2004) were reconstructed from the DWI data (spherical harmonic order 6) and peaks were extracted from the functions (density 100; search radius 0.4). To compare STIFT to the standard tractography alternative, PICo probabilistic tractography (Parker et al., 2003; Seunarine et al., 2007) was performed with and without STIFT adaptation. A constant seed for the random number generator was used.

Results

STIFT adaptation with the GE structure tensor

Diffusion weighted images and gradient echo magnitude images were coregistered by a carefully designed two-step coregistration and unwarping procedure (a qualitative impression of the result is provided in supplementary Figs. S1 and S2). A data-adaptive structure tensor was calculated from the GE image by applying an edge-enhancing diffusion filter. This filter was found to effectively remove small-scale spherical and tubular inhomogeneities (such as veins) from the GE image, while faithfully enhancing the sheet-like fiber bundles (Figs. 2ab). The cortex and venogram masks that were used are shown in Figs. 2d–f.

The structure tensor describes local image features by calculating the partial spatial derivatives of the smoothed image. The first eigenvector of the structure tensor captures the main orientation, or peak direction (PD_{GE}), of borders between white matter fiber bundles in the GE image at a high resolution (Fig. 3; green arrows). Along fiber bundles (e.g. at the outer border of the optic radiation, shown left in Fig. 3a) the PD_{GE} is approximately orthogonal to the Q-ball peak directions (PD_{DWI}: blue arrows). Nevertheless, there are varying degrees of mismatch between PD_{GE} and PD_{DWI}. This is best demonstrated by the difference between PD_{DWI} and the vectors after STIFT adaptation (PD_{STIFT}: red arrows). The STIFT adaptation (supplementary Fig. S3) rotated PD_{DWI} towards the edge between the fiber bundles in the GE image, making them more orthogonal to PD_{GE}. The first eigenvalue (Fig. 2c) is indicative of the contrast of the edge and determines the angle of rotation. The gain can be appreciated particularly well in Fig. 3b, where the Q-ball vectors are interpolated to the GE resolution. The resolution of the DWI is shown to be insufficient to capture the anatomy of the curved tracts, because the Q-ball vectors all show similar orientation. The STIFT vectors are better aligned with the fiber bundles and should lead to improvements in tractography.

STIFT vs. standard Q-ball tractography from closely spaced seed points

To investigate tracking behavior of STIFT at the border of two fiber tracts, STIFT was compared to standard probabilistic Q-ball tractography from seed pairs in close proximity (0.5 mm) on the border of 1) the optic radiation and inferior longitudinal fasciculus/inferior fronto-occipital fasciculus; and 2) the cingulum and corpus callosum. For comparison, seed pairs were also placed within these tracts (Figs. 4/5a).

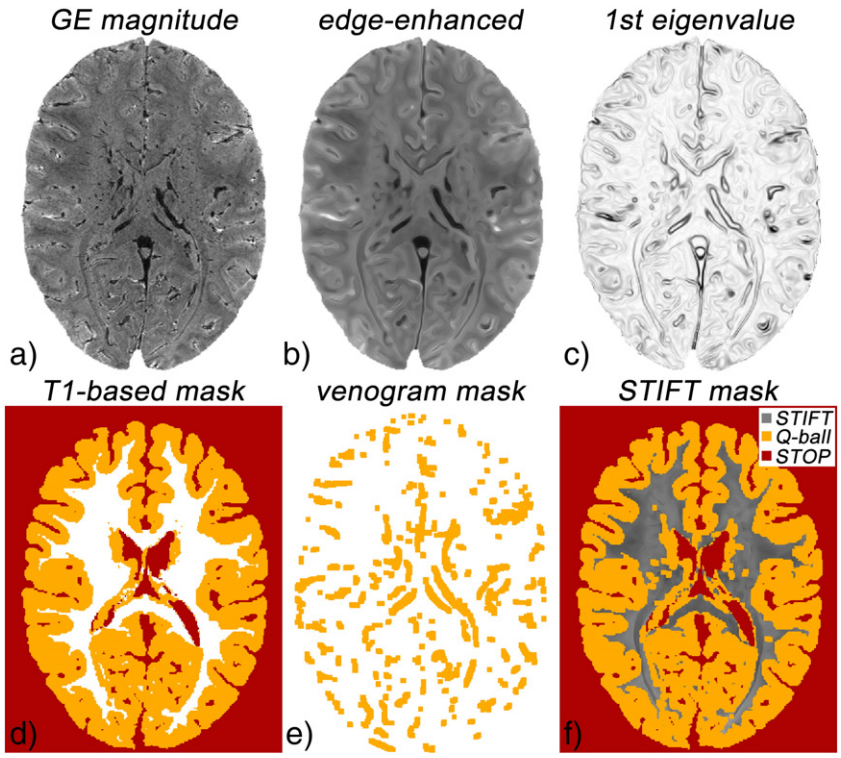

Fig. 2. Structure tensor filtering and masks. a) GE magnitude image; b) edge-enhanced GE image; c) first eigenvalue of the structure tensor; d) T1-based mask (WM–GM–CSF); e) GE-based mask (veins-slab profile); f) overlay of combined mask and edge-enhanced GE: gray: apply STIFT; orange: do not use STIFT; red: stop tracking.

The fibers from the seed pairs *on the border* of the tracts (Figs. 4/5e) show the most prominent difference between standard Q-ball-based and STIFT-based probabilistic tractography. Tracts are very mixed in the Q-ball results, while with STIFT the tracts from both seeds are clearly separated. Additionally, in the deep white matter the STIFT tracts stay closer to the tract border. The seed pairs placed *within* the tracts (Figs. 4/5df) are more similar for standard Q-ball and STIFT. STIFT results are considerably more mixed for adjacent seeds within the interior of the tracts, as compared to the seedpoint pairs on the tract border. Nevertheless, differences between Q-ball and STIFT are also seen for these pairs.

Occipitotemporal white matter

Tracking from the border of the optic radiation (Fig. 4e) with Q-ball (left panel), most of the fibers connect the calcarine sulcus (V1) to the temporal and frontal lobes, both for seeding inside (red fibers) and *outside* (blue fibers) the optic radiation. STIFT (right panel) shows endpoints in a more posterior portion of V1 and reconstructs part of Meyer's loop (white arrowhead) for the seed point placed within the OR (red fibers). The STIFT fibers tracked from the seedpoint in the ILF/IFOF (blue fibers) form a separate tract that connects extrastriate areas on the lateral aspect of the occipital lobe with temporal and frontal areas.

When seeding well within the OR (Fig. 4f; cyan/pink fibers), the STIFT tract (right panel) here includes both anterior and posterior V1 and features a sharper bend in Meyer's loop with a larger anterior extent. More fibers extend from V1 to temporal and frontal areas in the original Q-ball tractography (left panel) as compared to STIFT. When seeding in the ILF/IFOF (Fig. 4d; yellow/green fibers), fibers cross into the OR towards V1 for Q-ball (left panel) at the posterior end, but stay on the lateral side of the OR with STIFT (right panel). Anterior to the seed points, both Q-ball and STIFT connect to anterior temporal and superior parietal areas (not apparent in Fig. 4).

Frontoparietal white matter

The seedpoint pair at the border of cingulum and corpus callosum (Fig. 5e; red/blue fibers) gives rise to Q-ball fibers (left panel) running anteriorly in the cingulum, but with the vast majority of fibers showing a sharp bend coursing medially in the corpus callosum towards the contralateral hemisphere. These fibers cross-over from the cingulum to corpus callosum in the multifiber voxels at the border of these tracts (Fig. 5b). The same pattern is seen for the STIFT fibers from the seed within the cingulum (red fibers, right panel). From the corpus callosum seed (blue fibers), STIFT fibers (right panel) are tracked to the contralateral medial frontal cortex. Anteriorly, most fibers run parallel to the cingulum for a short distance in a u-fiber covering the cingulate sulcus to terminate in the ipsilateral medial frontal cortex.

For the seeds placed in the interior of the cingulum bundle (cyan/pink fibers) and corpus callosum (yellow/green fibers), fibers are mixed for adjacent seeds. However, standard Q-ball and STIFT results were not the same. What is immediately apparent for the fibers tracked from the seedpoints within the cingulum in Fig. 5f, is that Q-ball (left panel) tracks a large bundle of callosal fibers, while almost no corpus callosum fibers are tracked for STIFT (right panel). A second difference is that the anterior curve of the cingulum is extended over the rostrum for STIFT, while Q-ball shows more fibers fanning out into the frontal lobe (Fig. 5c). From the seedpoints in the corpus callosum, a u-shaped section of the corpus callosum is tracked for both standard Q-ball and STIFT. Ipsilateral from the seed, the same tracts are found for both techniques, but contralaterally Q-ball finds more tracts shooting off downward into the internal capsule and laterally towards dorsolateral prefrontal cortex.

Three seed point pairs were placed in the centrum semiovale where the corticospinal tract crosses the corpus callosum (Figs. 6ab). Results for standard Q-ball and STIFT (Figs. 6c–f) are similar for all seeds: most fibers follow the corona radiata and internal capsule, but some fibers also form a section of the corpus callosum. One qualitative

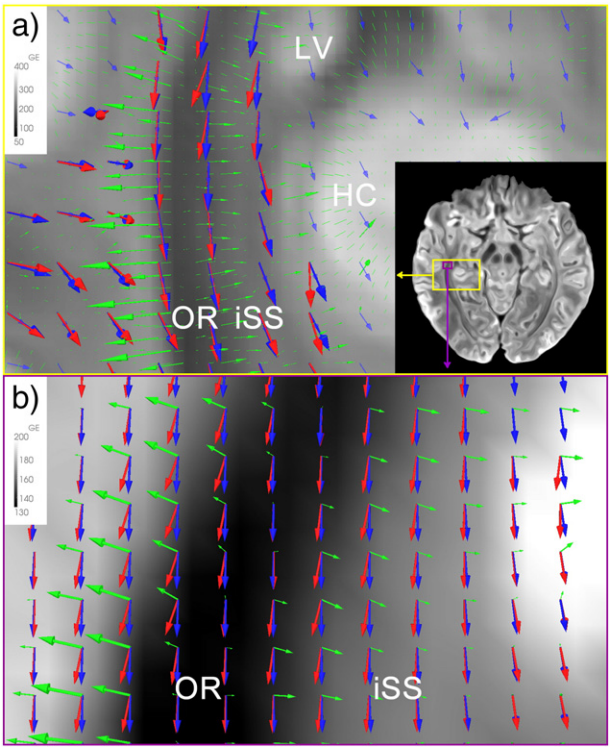

Fig. 3. STIFT adaptation. Shown are the structure tensor's 1st eigenvector (PD_{GE}: green arrows), Q-ball 1st peak direction (PD_{DWI}: blue arrows) and STIFT adaptation (PD_{STIFT}: red arrows) on an axial GE slice through the ventral optic radiation (Meyer's loop). a) STIFT adaptation performed at DWI voxel coordinates ($\Delta = 2$ mm). PD_{GE} is shown in native GE resolution, but only a random subset of vectors (within the WM mask) is shown as arrows. b) STIFT adaptation performed at GE voxel coordinates ($\Delta = 0.5$ mm). PD_{DWI} vectors are linearly interpolated. OR = optic radiation; iSS = internal sagittal stratum; HC = hippocampus; LV = lateral ventricle. Note that the STIFT vectors closely follow the structure of the optic radiation, whereas interpolated Q-ball vectors are not oriented along the tract.

difference is seen at the level of the internal capsule. While Q-ball fibers enter and pass through the lentiform nucleus, no STIFT fibers penetrate this nucleus. Instead, STIFT fibers typically stay contained within either the internal or external capsule.

Reconstruction of the optic radiation with STIFT and standard Q-ball

The optic radiation was tracked from seed regions lateral to the lateral geniculate nuclei to examine if the use of the structure tensor would improve reconstruction of the tract. Although the connectivity maps look similar at first glance (Fig. 7; left vs. middle column), the differences become most obvious by subtracting the Q-ball from the STIFT connectivity maps (right column). The whole-brain difference map of subject 1 (upper right panel) already shows that the voxels of the optic radiation contain more fibers for STIFT compared to Q-ball. Because the total number of initiated fibers is equal for both methods, Q-ball features more fibers in most other tracts to e.g. temporal, parietal and cerebellar regions. For subject 2, standard Q-ball tractography reconstructs a fiber bundle lateral to the OR that curves into the corpus callosum (obscuring the OR in the whole-brain difference image). However, if only fibers that connect to V1 are considered, it is clear that the tract volume of the left OR is dramatically increased for STIFT (fifth row).

With the changes in tract volume the morphology of the OR is also different, which is also reflected in the anterior extent of Meyer's loop (dotted lines). Both right and left OR of subject 1 show a larger anterior extent with STIFT,[1] although fewer fibers occupy the middle part of Meyer's loop in the right hemisphere. Meyer's loop was not found in the right hemisphere of subject 2 by either Q-ball or STIFT, whereas in the left OR the anterior extent is larger for STIFT compared to standard Q-ball.

Discussion

The results presented here demonstrate for the first time that DWI tractography can benefit from the incorporation of information from high-resolution structural images with contrast between white matter fiber bundles. The structure tensor was found to be a suitable representation of the gradient echo image, because it can be directly used to adapt the tracking direction in a tractography algorithm according to the contrast in the scalar image. Structure Tensor Informed Fiber Tractography is a useful and promising addition to the available tools to investigate white matter anatomy. STIFT has a number of advantages over current tractography methods, but in this developmental stage it also faces a number of challenges concerning the scope of its applicability.

Anatomy of reconstructed tracts

Occipitotemporal white matter

As the primary visual projection tract, the optic radiation (OR) is central to the occipitotemporal WM. The OR is entirely contained in the external sagittal stratum (Kitajima et al., 1996) and forms the geniculostriate pathway from the dorsal lateral geniculate nucleus (dLGN) to primary visual cortex (V1 or striate cortex) in the calcarine sulcus (Nieuwenhuys et al., 2008). In each hemisphere, the fibers from the contralateral lower quadrant of the visual field take a short pathway to the dorsal bank of the calcarine sulcus (the posterior bundle). The fibers that form the anterior bundle represent the contralateral upper quadrant and curve anteriorly over the roof of the ventricle to bend sharply in the temporal lobe (Meyer's loop) towards the ventral bank of the calcarine sulcus. The central bundle contains the foveal projection. It leaves the LGN in lateral direction and is wedged between the posterior and anterior bundles in its course towards the occipital pole (Conturo et al., 1999; Ebeling and Reulen, 1988; Nieuwenhuys et al., 2008).

Medial to the OR, the internal sagittal stratum contains corticofugal fibers from striate and extrastriate areas to various subcortical nuclei, including the dLGN and superior colliculus (Tusa and Ungerleider, 1988; Woodward and Coull, 1984) involved in visual reflexes. More medially still, the tapetum lines the lateral wall of the lateral ventricle, connecting the temporal lobes through the corpus callosum (Kitajima et al., 1996).

Although its existence as a bundle separate from the OR has been questioned (Tusa and Ungerleider, 1985), the inferior longitudinal fasciculus is thought to course lateral to the OR from extrastriate areas to the temporal lobe (Catani et al., 2003; Yeterian and Pandya, 2010). Similarly, the second association fiber bundle running lateral to the OR, the inferior fronto-occipital fasciculus (IFOF), has been disputed (Schmahmann and Pandya, 2007). However, the IFOF has been found in tractography (Catani et al., 2002) and dissection studies (Lawes et al., 2008; Martino et al., 2010) as a bundle running dorsal and posterior to the uncinate fasciculus in the frontal lobe and in between the optic radiation and ILF in temporo-occipital regions. Most laterally, a series of u-fibers known as the occipito-temporal projection system (Tusa and Ungerleider, 1985) form the indirect pathway of the visual ventral stream to the anterior temporal lobe.

[1] The loop extending far into the left temporal lobe for standard Q-ball does not match the anatomy of the OR, but forms an aberrant pathway lateral to the lateral ventricle (i.e. tapetum) and running posterior through the ILF. Similarly, some fibers are seen in the temporal lobe for STIFT that are not part of Meyer's loop.

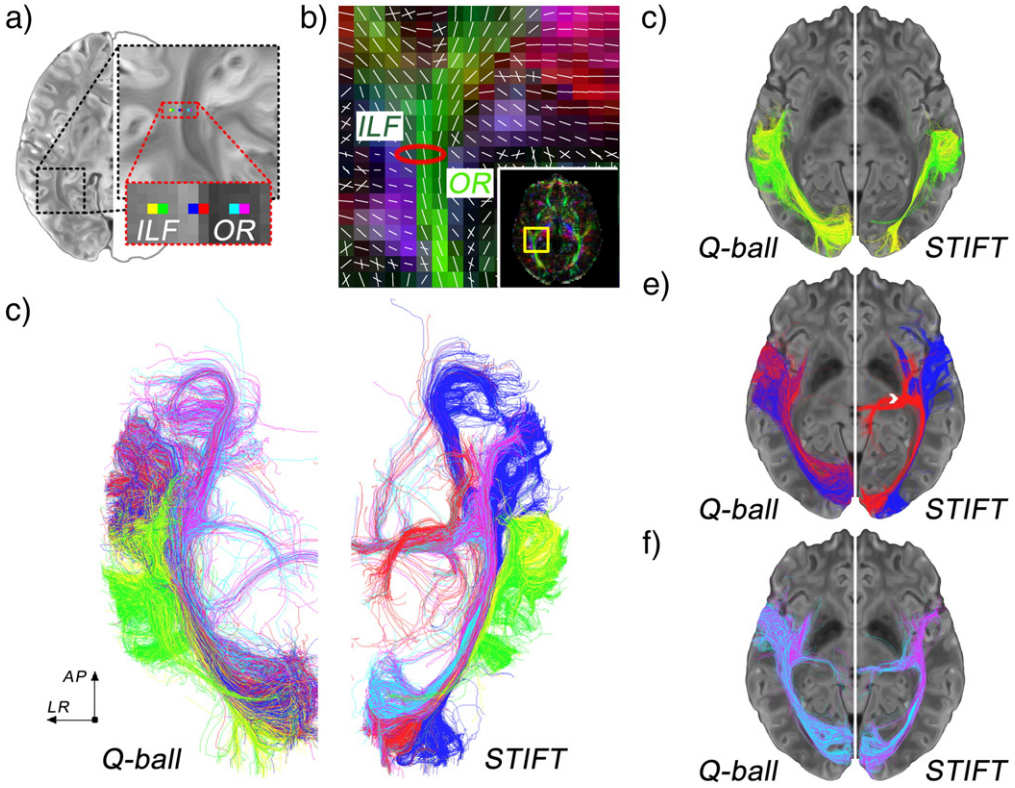

Fig. 4. Optic radiation (OR) and inferior longitudinal fasciculus/occipitofrontal (ILF) fiber tracts. a) Set of three seed pairs in the ILF (yellow/green) the OR (cyan/pink) and one pair on both sides of the border of these tracts (blue/red). b) Q-ball peak directions; red circle indicates the seed location (sagittal slice). c) Fiber tracts for Q-ball and STIFT (mirrored): composite image for all six seed points (ventral view). d,e,f) Fiber tracts for seed pairs in the ILF, on the border and in the OR, respectively (ventral view).

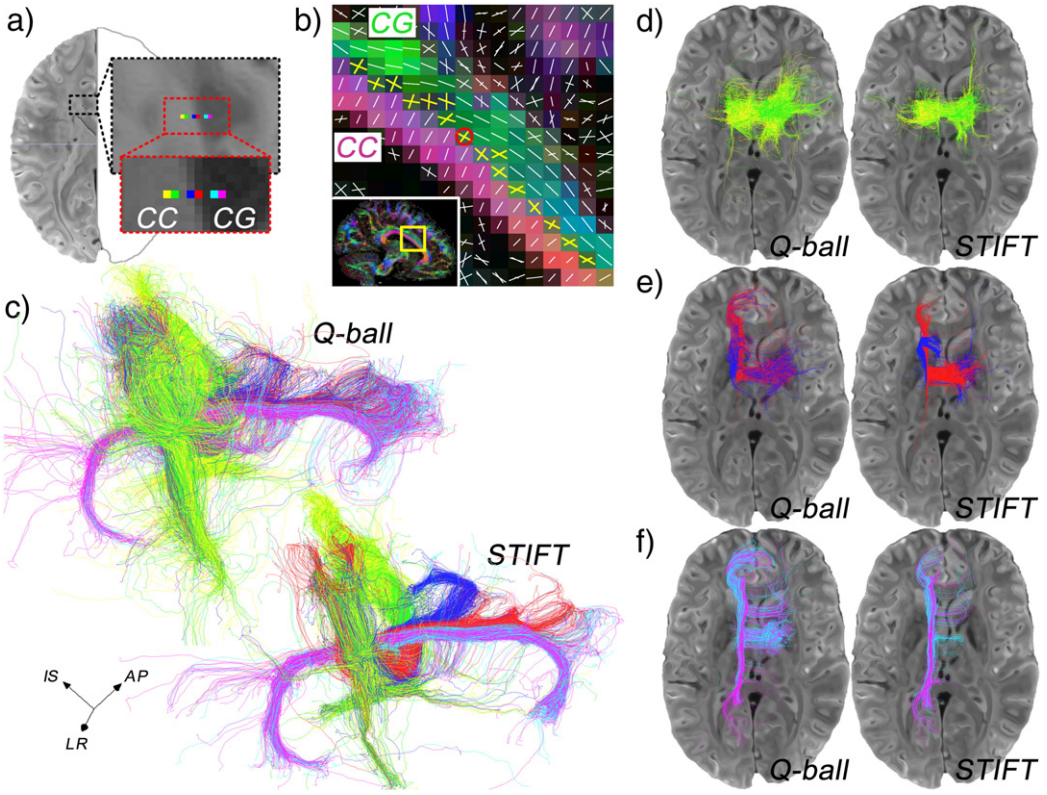

Fig. 5. Cingulum (CG) and corpus callosum (CC) fiber tracts. a) Set of three seed pairs in the CC (yellow/green) the CG (cyan/pink) and one pair on both sides of the border of these tracts (blue/red). b) Q-ball peak directions with multifiber voxels (yellow crosses) at the border of the CG and CC; red circle indicates the seed location (sagittal slice). c) Fiber tracts for Q-ball and STIFT: composite image for all six seed points. d,e,f) Fiber tracts for seed pairs in the CC, on the border and in the CG, respectively (dorsal view).

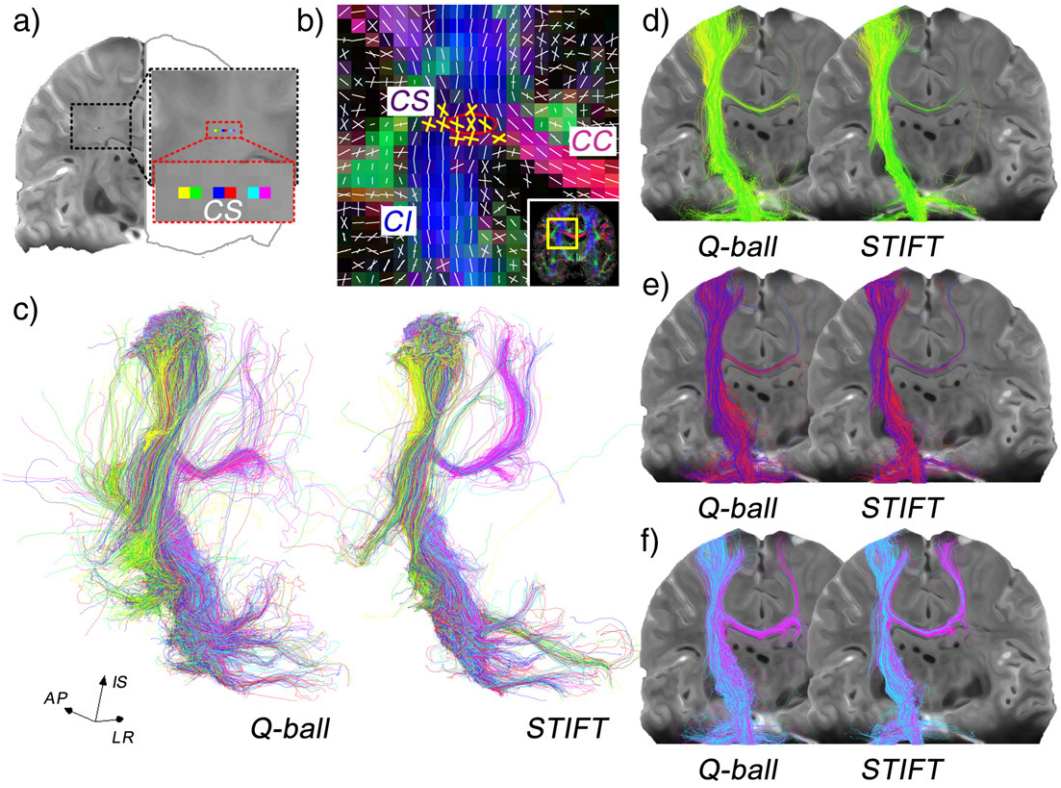

Fig. 6. Corticospinal and corpus callosum fiber tracts. a) set of three seed pairs in the centrum semiovale (CS). b) Q-ball peak directions with multifiber voxels (yellow crosses) in the CS where internal capsule (CI) fibers cross with corpus callosum (CC) fibers; red oval indicates the seed location. c) Fiber tracts for Q-ball and STIFT: composite image for all six seed points. d,e,f) Fiber tracts for seed pairs in the CS (posterior view).

To illustrate the behavior of STIFT in comparison to Q-ball, neighboring seed points ($\Delta x = 0.5$ mm) were chosen in the OR and ILF/IFOF and on the border of these tracts. The seed pair *on the border* showed the most distinct differences, as could be expected from the STIFT algorithm weighing the structure tensor by edge strength. For Q-ball, tracts from both seeds in the border pair (i.e. in the OR and ILF/IFOF) were very similar, connecting the anterior part of V1 with anterior temporal and lateral frontal regions. Because long-range cortico-cortical association tracts from *primary* sensory areas are absent in humans and primates (Felleman and Van Essen, 1991; Geschwind, 1965), the Q-ball result represents a tract that erroneously connects the anterior endpoints of the ILF/IFOF with the posterior endpoint of the OR. The STIFT results showed a different pattern, with clearly separated tracts for both seeds in the pair. Most fibers from the seed in the OR extended to the posterior part of V1, while anterior to the seed point most fibers coursed medially into the thalamus, forming part of Meyer's loop. This tract is in accordance with the known anatomy of the OR. From the border seed in the ILF/IFOF, STIFT fibers extend to *extra*striate areas on the lateral aspect of the occipital lobe. Anteriorly, fibers terminate in the anterior temporal and lateral frontal lobes. The ILF is indeed defined as the tract connecting extrastriate areas with anterior temporal areas (Catani et al., 2003), whereas the IFOF extends from extrastriate to lateral frontal regions (Martino et al., 2010). Therefore, STIFT finds plausible occipito-temporal and occipito-frontal pathways from the ILF/IFOF seedpoint.

Tracking from the seed pair within the OR, Q-ball shows similar V1-frontotemporal connections as were found from the seed pair on the border, but a small percentage of fibers now terminates in the thalamus, finding part of Meyer's loop. Although this presents an improvement over the OR border seedpoint, seeding in the middle of the OR is expected to connect a larger amount of fibers to the thalamus. For STIFT, Meyer's loop is found to have a sharper bend and more fibers as compared to the Q-ball results.

In contrast to the seed on the lateral border of the OR, fibers from the seed pair within the OR terminate in the *anterior* part of V1, on the *ventral* bank of the calcarine sulcus. Also, these fibers show a larger anterior extent in Meyer's loop and are inferior to the tract from the OR border seed in this area. These characteristics suggest that the fibers from the seed pair within the OR form part of the anterior bundle of the optic radiation. On the other hand, the STIFT tract from the OR border seedpoint resembles the central bundle of the OR: it exits the LGN in lateral direction and terminates in the occipital pole. This is consistent with the topography of the optic radiation described by Ebeling and Reulen (1988). Ebeling and Reulen also observed that the posterior and anterior bundles are not completely separated by the central bundle over the course of the OR. Instead, at the level of the trigone of the lateral ventricle "the macular fibres lie rather lateral in a base-out wedge between the fibres of the anterior and posterior bundle". The OR seedpoints were indeed placed at this level in the present study. Therefore, it is likely that the OR border seedpoint was placed within the 'wedge' of the central bundle, while the medial seed pair within the OR was placed within the anterior bundle.

The seed pair contained within the ILF/IFOF tracks occipito-temporal and temporo-parietal connections for both Q-ball and STIFT. Some differences, however, were observed. Many fibers are tracked into V1 for Q-ball, whereas most fibers connect to extrastriate regions for STIFT. As indicated before, the ILF is thought to connect extrastriate cortex to the temporal lobe. The absence of frontal fibers for both methods suggests that the placement of this seed pair is not in the IFOF, which is in accordance with the IFOF as a very thin sheet of fibers directly lateral to the OR (Martino et al., 2010). Furthermore, Q-ball shows more branches towards lateral parietal cortex, while STIFT fibers mostly terminate in anterior temporal regions. Whether the seed pair is truly placed within the ILF or in the area of u-fibers cannot be established with confidence.

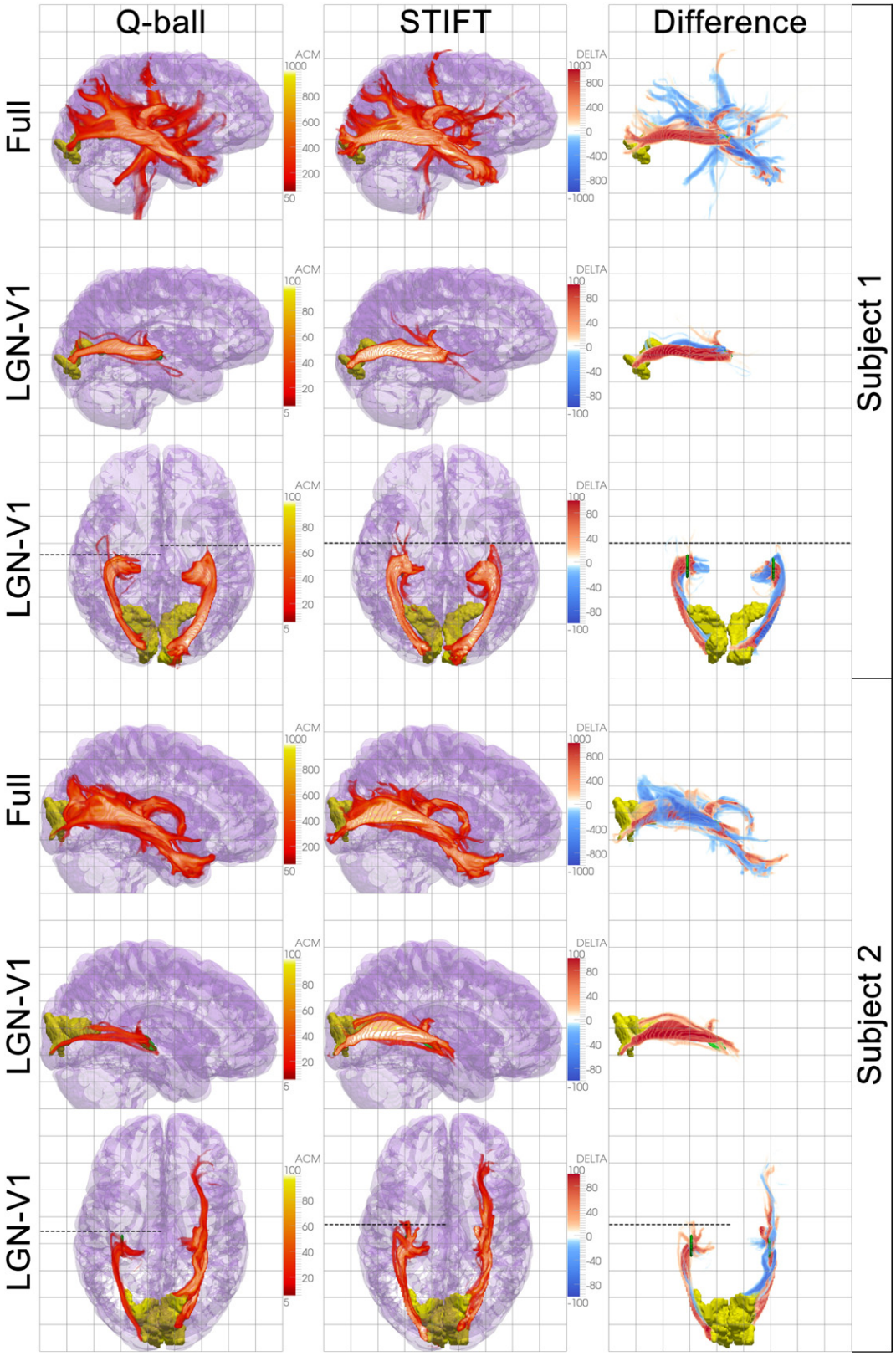

Fig. 7. Anatomical connectivity maps. Comparison between Q-ball (left column) and STIFT (middle column). The right column shows the difference maps, where red tracts indicate more fibers for STIFT compared to Q-ball and blue tracts indicate more fibers for Q-ball vs. STIFT. Upper panels for each subject show connectivity from the left seed region (green). The middle and lower panels show the tracts from the seed regions to the pericalcarine cortex (yellow) in lateral (only left OR shown) and ventral views, respectively. LGN-V1 tracts are truncated medial and anterior to the LGN. Dotted lines indicate furthest extension of Meyer's loop.

Tractography from the seed regions lateral to the LGN resulted in similar *overall* patterns of connectivity for both techniques, indicating that the major tracts going through the seed region can be found with both techniques. On the other hand, STIFT results were different from the Q-ball results in a number of important aspects.

The balance between the fiber counts in various tracts is shifted in favor of the OR when using STIFT. The OR fibers gained with STIFT were distributed over all other tracts with Q-ball. This shift in balance in favor of the OR can be regarded as a positive result, as the seed region was specifically selected to capture the OR fiber bundle. However, the interpretation of quantitative measures of tractography, such as fiber count, is not straightforward. From the anatomical perspective, fiber count in tractography is easily mistaken for (a measure of) number of axons in the tract. From the connectivity perspective, fiber counts are used as a measure for the probability of the existence of a connection. Although our results show similar connectivity patterns for both Q-ball and STIFT, the connectivity fingerprint (Passingham et al., 2002) differs in magnitude over its connections. Whether STIFT connection probabilities represent an improvement over traditional methods is an open question. At this proof-of-principle stage, STIFT lacks the formal model available for some other probabilistic methods (Behrens et al., 2003; Parker et al., 2003) to perform a proper analysis of connection probability.

In light of e.g. presurgical planning, tract volume—which was found to be underestimated by deterministic tractography (Thiebaut de Schotten et al., 2011)—and the exact morphology of the tracts are more informative than fiber count. Selecting the OR only (by excluding the fibers not connecting to V1) showed improvements for STIFT in both aspects. STIFT showed increased tract volume, in particular for one hemisphere where standard Q-ball only reconstructed a minor part of the tract.

The anterior extent of Meyer's loop displays a large intersubject variability, but is generally thought to cover the tip of the temporal horn of the lateral ventricle (Ebeling and Reulen, 1988). Although this extent was not found in our subjects, STIFT fibers coursed more anteriorly in comparison to Q-ball fibers in three of the four hemispheres investigated (in the fourth, both Q-ball and STIFT failed to find Meyer's loop).

Frontoparietal white matter

In the frontoparietal WM, we investigated multifiber voxels in adjacent and crossing fiber bundles. The corpus callosum (CC) and cingulum (CG) are assumed to be adjacent (kissing) fiber bundles (Tournier et al., 2011). The nearby centrum semiovale (CS) contains crossing (interdigitating) fibers of several tracts, including the corticospinal tract (CST) and corpus callosum (Tournier et al., 2011).

The corpus callosum is a massive interhemispheric fiber pathway. The medial segments of the CC fibers of the frontoparietal white matter are contained in the body of the corpus callosum: the section that forms the roof of the lateral ventricles. Fibers of the body of the CC fan out into the hemispheres bending dorsally to medial frontoparietal areas, but fibers also fan out towards cortical areas on the lateral aspect of the hemisphere. On their way from midline to lateral cortex, the fibers of the body of the CC traverse several other fiber tracts. In the area known as the centrum semiovale, the CC fibers cross the fibers from the internal capsule that also radiate out over the hemispheres as the corona radiata. Additionally, association fibers (e.g. the superior longitudinal fasciculus) run through the area in anteroposterior direction (Nieuwenhuys et al., 2008).

Dorsal to the corpus callosum, just lateral to the midline, the cinguli are encapsulated on three sides by the cingulate gyri. In the sagittal plane, cingulum fibers arch over the full anteroposterior extent of the medial corpus callosum. At the isthmus of the cingulate gyrus, the cingulum turns sharply around the splenium of the corpus callosum to course within the parahippocampal gyrus towards the limbic areas of the medial temporal lobes (Nieuwenhuys et al., 2008). The lateral border of the cingulum verges on the dorsal corpus callosum that curls upward from the midline to medial frontoparietal cortical areas. These fibers are thought to be a good example of a kissing fiber configuration (Tournier et al., 2011).

Similar to the approach in the occipitotemporal WM, we placed seed point pairs on the border of the cingulum and corpus callosum, and in the interior of both tracts. Assuming that the cingulum and corpus callosum are kissing fiber tracts, the seeds in the cingulum should reconstruct the cingulum only, without fibers crossing-over into the corpus callosum and vice versa. However, due to the ambiguity of fiber configurations in multifiber voxels probabilistic algorithms often connect segments of separate tracts, thus creating false positives. False negatives, on the other hand, result from inability to traverse crossing fiber areas due to dominance of the fiber traversed (Tournier et al., 2011). Both were observed in our results, but to different degrees for standard Q-ball and STIFT.

For Q-ball, we observed substantial cross-over for all seeds within the cingulum and for the border seed within the corpus callosum. Anterior to the border seeds, the cingulum was tracked. In the other segment most fibers crossed-over to the corpus callosum. The seeds within the interior of the cingulum correctly reconstructed the cingulate part of the cingulum, but at the coronal level of the seedpoint the typical u-shaped dorsal section of the CC was also tracked. STIFT presented a modest improvement for the border seeds, but a substantial improvement for the seeds within the interior of the cingulum. From the cingulum border seed, a number of STIFT fibers were tracked towards the posterior end of the cingulum, but a majority of fibers still followed the CC. The STIFT fibers from the corpus callosum border seed did not enter the cingulum, but ran parallel to it within a u-fiber in the seeding hemisphere (Q-ball results showed a mixture between anterior cingulum and u-fibers). In short, with STIFT we observe a reduced false positive rate connecting segments of the CC with the CG. The substantial callosal segment reconstructed with Q-ball tractography from the seeds in the interior of the cingulum is likely to be an artifact of tracking through partial volume CC/CG voxels. Note, however, that it cannot be excluded—and it is even likely—that some cingulum fibers enter the corpus callosum (Locke and Yakovlev, 1965) to form heterotopic transcallosal connections. The two-fiber configuration on the CC/CG border might therefore not be completely attributable to partial volume of the tracts, but also to a contribution of crossing fibers.

The cingulum bundle was longer for STIFT compared to Q-ball, extending over the genu of the corpus callosum. This is indeed the extent described in textbooks (Nieuwenhuys et al., 2008). However, a reduction in fibers aggregating from and fanning out into the frontal lobe was also seen. As it is known that the cingulum is also a fiber complex that includes fibers other than from the cingulate gyrus itself (e.g. connections from prefrontal to parahippocampal regions (Goldman-Rakic et al., 1984)), the cingulum extension might represent an improvement in tractography at the cost of true positives fibers.

For comparison with the kissing fiber situation, we compared STIFT to standard Q-ball for tractography from seeds within a crossing fiber area: the centrum semiovale, where the corticospinal tract crosses the corpus callosum. As could be expected, the effect of STIFT was negligible in this area. Because the edge-enhanced GE image is relatively homogeneous in the centrum semiovale, it is not expected that STIFT provides additional guidance in this area. The anatomy of the tracts *outside* the region of the centrum semiovale did show some differences between standard Q-ball and STIFT. First, most Q-ball fibers entering the corpus callosum terminated at the contralateral centrum semiovale. STIFT fibers were tracked more often to contralateral medial frontoparietal cortex, following one of the anatomically likely fiber pathways. Second, the CST reconstructed with STIFT was narrower as compared to the Q-ball CST: STIFT fibers were contained in the internal capsule, but Q-ball fibers also entered the surrounding nuclei (with more fibers radiating back into the internal capsule/corona radiata). STIFT fibers did not enter the nuclei, as a result of the strong contrast between the internal

capsule and, in particular, the lentiform nucleus. In the present example, STIFT can be considered an improvement in the representation of the morphology, because the seeds were placed inferior to the primary motor cortex to track the CST. The CST is composed of fibers that aggregate from the full mediolateral extent of the primary motor cortex, but that form a narrow bundle within the posterior limb of the internal capsule to descend directly into the spinal cord (Nieuwenhuys et al., 2008). It should be acknowledged that this is a rather special case, where the subcortical nuclei are not targets for tractography (see Limitations).

Benefits of STIFT

Spatial resolution

The primary advantage of STIFT is the fine spatial scale at which fiber tracts can be distinguished. At the substantially higher resolution of the GE voxel (64×) compared to typical DWI voxels, much more detail of the macroanatomical architecture can be captured. This was specifically shown for the bending fiber sheet of the optic radiation (Fig. 3b), but the principle extends to identification of smaller tracts (e.g. the anterior commissure could be easily identified in our GE images, but not in our color-coded FA images) and reduced partial volume of separate fiber tracts. In current tractography methods, diffusion vectors are available on a coarsely sampled grid that is generally interpolated to arrive at the tracking direction at a certain point. In STIFT, this spatially coarsely sampled directional information is complemented by detailed anatomical knowledge about the course of the fiber bundles. The STIFT implementation presented in the current paper penalizes tractography in the directions of edges in the image, which are assumed perpendicular to fiber tracts. The penalty is weighted by the dissimilarity between the tracts (i.e. the gradient magnitude), using it as a measure of evidence that particular GE voxels belong to the same or a different tract. This has benefits that manifest in a number of ways.

First, tracking a fiber near the tract border closely follows the course of the fiber bundle with STIFT, while current algorithms can miss bends in a tract. Therefore, anatomical accuracy of fiber bundle morphology is increased with STIFT.

Second, fibers will not easily cross over to the other tract, but stay close to the tract border. Consequently, by virtue of the considerable higher resolution of the GE image compared to the DWI, STIFT provides a much better tract separation in locations where this is appropriate.

Third, STIFT fiber bundles diverge less around tract borders as compared to the Q-ball counterpart. The method presented here reduces uncertainty in the fiber direction using the assumptions that fibers at tract borders course parallel to fiber sheets in GE image (Röttger et al., 2011) and strong T_2^*-contrast represents a fiber boundary. In areas where GE contrast is absent or masked, STIFT falls back on the original tracking behavior. Hence, fibers are allowed to splay where the GE contrast decreases (e.g. near V1 in the optic radiation), while tracts are narrow and well defined around the borders.

Fourth, STIFT favors longer tracts, because fibers tend to remain within long-range fiber bundles (e.g., the anterior extension of the cingulum bundle in Fig. 5c). This presents another advantage over the current probabilistic tractography methods. In probabilistic tractography, connection probabilities decrease with distance to the seedpoint due to propagation of uncertainty in the diffusion measurement in each step of the tracking process (Behrens et al., 2003; Jones, 2003), thereby overestimating short-range connections (Gigandet et al., 2008; Morris et al., 2008). STIFT reduces uncertainty as a result of the combination of DWI and GE information and increases tract coherence by aligning tracking directions along the tract.

Adjacent vs. crossing tracts

A secondary advantage of STIFT is that it uses an independent source of information complementary to DWI. As was demonstrated in the present paper, this can be especially valuable in distinguishing the underlying fiber distribution in some of the multifiber voxels in the brain. In principle, the GE image can provide information to distinguish between crossing and adjacent tracts if the tracts have different susceptibilities or orientations. Adjacent tracts with a difference in susceptibility that 'kiss' (e.g. cingulum and corpus callosum) are characterized by an intensity gradient between them, while tract crossings where fibers of different tracts interdigitate (e.g. centrum semiovale) would result in an area of average susceptibility. Therefore, in a multifiber voxel that contains kissing tracts with different susceptibilities, STIFT penalizes crossing over to the other tract. This was seen in our example of the cingulum where it touches the corpus callosum. Standard Q-ball showed a crossing-over for many fibers from cingulum to corpus callosum when seeded in the cingulum. STIFT presented an improvement. Fibers seeded in the interior of the cingulum remained in the cingulum and STIFT fibers seeded in the corpus callosum did not yield any cingulum fibers. Note, however, that STIFT is not expected to be beneficial for resolving crossing tracts.

Limitations

Some limitations of STIFT have also to be noted. The structure tensor is not equally informative throughout the brain. First, the GE image contrast is not equal for all tracts, but is strongest for some of the major fiber bundles. Other tracts may not differ in susceptibility, or contrast-to-noise ratio may not be sufficient to detect modest susceptibility differences.

This preliminary investigation focused on STIFT employing the GE magnitude image. The R_2^* map obtained from multi-echo GE acquisitions is an appealing alternative, because it is less prone to artifacts and there would be no need for bias field correction (Denk and Rauscher, 2010). As the phase image also shows WM heterogeneity with an even higher contrast-to-noise ratio, it is also an excellent candidate for STIFT. Moreover, a susceptibility weighted image (Haacke et al., 2004) calculated by using a phase mask constructed specifically to enhance WM contrasts might be optimal. However, phase images also contain non-local effects that can lead to voxel intensities that are not representative of the local tissue and thus, an incorrect structure tensor. Lately, considerable efforts have been made to reconstruct quantitative susceptibility maps (QSM) from the GE phase data (de Rochefort et al., 2010; Liu et al., 2009; Schweser et al., 2011). This seems promising for obtaining more accurate, whole brain representations of the fiber bundles not affected by non-local effects. Susceptibility Tensor Imaging (Liu, 2010) also holds some promise in the combination with DWI, but with its requirement of many head rotations it is very cumbersome to obtain in vivo. It has the advantage that the tensor-valued image is informative in the tract's interior as well.

Furthermore, the GE white matter contrast has multiple sources: an orientation-dependent component and a susceptibility-dependent component. These sources of contrast could enhance or counteract each other. On the one hand, the orientation-dependent contrast can be used to separate tracts where neighboring tracts have different orientations. On the other hand, a single tract that shows a sharp bend could show an intensity gradient within the tract due to the GE orientation sensitivity.

Similarly, susceptibility might not be homogeneous along a tract. The STIFT method assumes that intensity gradients in the GE magnitude image represent contrast between different fiber bundles. However, within-tract R_2^* variation has already been described for some of the larger fiber bundles (Cherubini et al., 2009). Variations within a tract (e.g. in iron concentration or myelination) are likely to be much more gradual as compared to variations between two different tracts. This is certainly true for the optic radiation that appears well defined on the GE image, especially on its lateral border. Nevertheless, tract bends, crossings and susceptibility variations in the

direction of the tract can manifest as a small gradient oriented along the tract. In the presence of a larger gradient between tracts this will make the structure tensor more isotropic, but will not affect its first eigenvector as long as the within-tract gradient is smaller than the between-tract gradient. At least for the tracts investigated in the present paper, we did not experience problems due to contrast along the tracts. Even though the corpus callosum clearly has lower intensity than the centrum semiovale, no negative effects were experienced in tracking the crossing fibers of the corticospinal tract and corpus callosum.

Contrasts in GE images that do not originate from susceptibility differences between white matter tracts have to be considered when using STIFT. For example, because of the GE gray-white matter contrast the structure tensor is oriented radially at gray-white matter boundaries, thus potentially preventing fibers from entering the target gray matter. Therefore, a mask was used to prevent the STIFT adaptation at the GM-WM border of the cortex. The mask covered the entire cortical GM–WM border, but did not completely cover the subcortical gray matter, including some nuclei with short T_2^* (i.e. substantia nigra, red nuclei and lentiform nuclei). For the optic radiation and cingulum, this is unlikely to have influenced our results, because the tracts investigated did not terminate or cross these nuclei. However, for the internal capsule, which runs between the lentiform nucleus and thalamus, the effect of the nuclei was evident. Standard Q-ball tracked through the lentiform nucleus, while STIFT fibers coursed within the internal and external capsules and did not enter the nucleus. For connectivity analyses that include the subcortical nuclei this would be highly undesirable. Therefore, careful masking of subcortical structures is required when STIFT is used for this purpose. A second source of non-white matter contrast is the ubiquitous presence of venous vessels in the GE image. To address these, a filter was used that smoothed small veins, while fiber sheets were enhanced. Furthermore, an MR venogram was used as a vessel mask for the larger veins as a second mitigation strategy. The necessity of masking the vessels and CSF can even be questioned, because the structure tensor might in fact be beneficial in these locations as—in principle—it is undesirable to track into vessels or CSF. However, in this first demonstration of the method we chose to focus on white matter contrast, because the vessel contrast is very large compared to white matter contrasts and susceptibility effects can extend outside the veins.

A more practical issue concerns the use of two MRI systems. The T_2^* contrast in the GE image increases with field strength (Gati et al., 1997) and white matter heterogeneity is much less at 3 T compared to 7 T, although the optic radiation is also detectable at 3 T (Mori et al., 2009). While 7 T might be optimal for the GE image, it is challenging to obtain high quality DWI at this field strength. Fortunately, 7 T DWI sequences suitable for *in vivo* brain imaging are a topic of active investigation (Heidemann et al., 2010). Single-session STIFT is within reach, because DWI at 7 T with an acceptable image quality and acquisition time should be realized in the near future.

Conclusions

We developed Structure Tensor Informed Fiber Tractography as a tool to improve tracking of fiber pathways through the brain. The structure tensor of the gradient echo image informs about the course of fiber bundles at a resolution that is not yet within reach for whole-brain *in vivo* diffusion weighted imaging. The fiber bundles obtained with probabilistic tractography from seedpoints in the optic radiation, inferior longitudinal fasciculus and cingulum are in better agreement with known anatomy for STIFT as compared to standard Q-ball based tractography. Fiber tracts are well separated for closely spaced seed points in neighboring tracts, forming narrow bundles in locations where the GE image can provide the detailed morphology of the tract. The benefits of STIFT can be mainly attributed to the high resolution of the GE image, but it has been shown that STIFT is also able to distinguish kissing from crossing tracts within a DWI voxel. Advances in anatomical gradient echo imaging, such as quantitative susceptibility mapping and susceptibility tensor imaging, and diffusion imaging at high field strengths is expected to further broaden the scope of applicability of STIFT to more fiber tracts.

Supplementary materials related to this article can be found online at doi:10.1016/j.neuroimage.2011.10.078.

Acknowledgments

This work was financially supported by the Dutch Ministerie van Economische Zaken, Provincie Overijssel and Provincie Gelderland through the ViP-BrainNetworks project.

Appendix A

The structure tensor was calculated by the following procedure from Kroon and Slump (2009) (http://www.mathworks.com/matlabcentral/fileexchange/25449-image-edge-enhancing-coherence-filter-toolbox):

1) The image I_t is smoothed with Gaussian kernel K_σ:

$$I_\sigma = K_\sigma * I_t$$

2) The structure tensor J_t is calculated by the outer product of the gradients of I_σ:

$$J_t = \nabla I_\sigma \nabla I_\sigma^T = \begin{pmatrix} I_{\sigma_x}^2 & I_{\sigma_{xy}} & I_{\sigma_{yz}} \\ I_{\sigma_{yx}} & I_{\sigma_y}^2 & I_{\sigma_{yz}} \\ I_{\sigma_{zx}} & I_{\sigma_{zy}} & I_{\sigma_z}^2 \end{pmatrix}$$

3) The tensor components are smoothed with Gaussian kernel K_ρ:

$$J_\rho = K_\rho * J_t$$

4) J_ρ is decomposed in eigenvectors $[\mathbf{v}_1, \mathbf{v}_2, \mathbf{v}_3]$ and eigenvalues $[\mu_1, \mu_2, \mu_3]$;

5) To preferentially smooth along planar edges, the diffusion tensor D is constructed as $[\mathbf{v}_1, \mathbf{v}_2, \mathbf{v}_3]$ with eigenvalues:

$$\lambda_1 = \alpha$$

$$\lambda_2 = \alpha + (1-\alpha)^{\frac{-C}{(\mu_2-\mu_3)^{2m}}}$$

$$\lambda_3 = \alpha + (1-\alpha)^{\frac{-C}{(\mu_1-\mu_3)^{2m}}}$$

6) The image I_t is updated by:

$$I_{t+dt} = I_t + \partial I_t dt$$

numerically approximating the diffusion equation

$$\frac{\partial I_t}{\partial t} = \nabla\cdot(D\nabla I_t)$$

with an explicit rotation-invariant finite difference scheme proposed by Weickert and Scharr (2002) and extended to 3D by Kroon and Slump (2009):

$$\nabla\cdot(D\nabla I_t) = \partial_x j_1 + \partial_y j_2 + \partial_z j_3$$

and

$$j_1 = D_{xx}\cdot(\partial_x I_t) + D_{xy}\cdot\left(\partial_y I_t\right) + D_{xz}\cdot(\partial_z I_t)$$

$$j_2 = D_{yx}\cdot(\partial_x I_t) + D_{yy}\cdot\left(\partial_y I_t\right) + D_{yz}\cdot(\partial_z I_t)$$

$$j_3 = D_{zx}\cdot(\partial_x I_t) + D_{zy}\cdot\left(\partial_y I_t\right) + D_{zx}\cdot(\partial_z I_t)$$

calculating the derivates by convolution with a Sobel kernel with a Scharr-valued 3D stencil.

7) Steps 1–5 are iterated until t = T;
8) At t = T, the final structure tensor is recalculated without Gaussian smoothing:

$$J_T = \begin{pmatrix} {I_T}^2{}_x & I_{T_{xy}} & I_{T_{yz}} \\ I_{T_{yx}} & {I_T}^2{}_y & I_{T_{yz}} \\ I_{T_{zx}} & I_{T_{zy}} & {I_T}^2{}_z \end{pmatrix}$$

9) J_T is decomposed in eigenvectors and eigenvalues.[2]

For filtering the GE magnitude images $\sigma = 1$, $\rho = 1$, $dt = 0.1$ s, $T = 10$ s, $C = 1\cdot10^{-10}$, $\alpha = 1\cdot10^{-3}$ and $m = 1$ were used. These values were determined experimentally to preserve edges between target fiber bundles and thus maintain the accurate localization of white matter fiber sheets, while giving a smooth structure tensor field not corrupted by small artifacts (e.g. veins) and noise in the data.

References

Basser, P.J., Mattiello, J., LeBihan, D., 1994. MR diffusion tensor spectroscopy and imaging. Biophys. J. 66, 259–267.

Beaulieu, C., 2002. The basis of anisotropic water diffusion in the nervous system — a technical review. NMR Biomed. 15, 435–455.

Behrens, T.E.J., Woolrich, M.W., Jenkinson, M., Johansen-Berg, H., Nunes, R.G., Clare, S., Matthews, P.M., Brady, J.M., Smith, S.M., 2003. Characterization and propagation of uncertainty in diffusion-weighted MR imaging. Magn. Reson. Med. 50, 1077–1088.

Bender, B., Klose, U., 2010. The in vivo influence of white matter fiber orientation towards B0 on T2* in the human brain. NMR Biomed. 23, 1071–1076.

Brox, T., van den Boomgaard, R., Lauze, F., van de Weijer, J., Weickert, J., Mrázek, P., Kornprobst, P., 2006. Adaptive structure tensors and their applications. In: Weickert, J., Hagen, H. (Eds.), Visualization and Processing of Tensor Fields. Springer Berlin, Heidelberg, New York.

Calamante, F., Tournier, J.D., Jackson, G.D., Connelly, A., 2010. Track-density imaging (TDI): super-resolution white matter imaging using whole-brain track-density mapping. NeuroImage 53, 1233–1243.

Catani, M., Howard, R.J., Pajevic, S., Jones, D.K., 2002. Virtual *in vivo* interactive dissection of white matter fasciculi in the human brain. NeuroImage 17, 77–94.

Catani, M., Jones, D.K., Donato, R., ffytche, D.H., 2003. Occipito-temporal connections in the human brain. Brain 126, 2093–2107.

Cherubini, A., Péran, P., Hagberg, G.E., Varsi, A.E., Luccichenti, G., Caltagirone, C., Sabatini, U., Spalletta, G., 2009. Characterization of white matter fiber bundles with T2* relaxometry and diffusion tensor imaging. Magn. Reson. Med. 61, 1066–1072.

Conturo, T.E., Lori, N.F., Cull, T.S., Akbudak, E., Snyder, A.Z., Shimony, J.S., McKinstry, R.C., Burton, H., Raichle, M.E., 1999. Tracking neuronal fiber pathways in the living human brain. Proc. Natl. Acad. Sci. U. S. A. 96, 10422–10427.

Cook, P.A., Bai, Y., Nedjati-Gilani, S., Seunarine, K.K., Hall, M.G., Parker, G.J., Alexander, D.C., 2006. Camino: open-source diffusion-MRI reconstruction and processing. 14th Scientific Meeting of the International Society for Magnetic Resonance in Medicine. Seattle, WA, USA, p. 2759.

Cook, P.A., Symms, M., Boulby, P.A., Alexander, D.C., 2007. Optimal acquisition orders of diffusion-weighted MRI measurements. J. Magn. Reson. Imaging 25, 1051–1058.

Dale, A.M., Fischl, B., Sereno, M.I., 1999. Cortical surface-based analysis. I. Segmentation and surface reconstruction. Neuroimage 9, 179–194.

de Rochefort, L., Liu, T., Kressler, B., Liu, J., Spincemaille, P., Lebon, V., Wu, J., Wang, Y., 2010. Quantitative susceptibility map reconstruction from MR phase data using Bayesian regularization: validation and application to brain imaging. Magn. Reson. Med. 63, 194–206.

[2] To achieve similarity in nomenclature in the main text between DWI and GE vectors, the peak directions in the DWI data are referred to as PD_{DWI}, while the peak direction of an edge in the edge-enhanced GE image—the main orientation—is referred to as PD_{GE}. The corresponding (largest) eigenvalue is called $\lambda_{PD_{GE}}$.

Thiebaut de Schotten, M., Ffytche, D.H., Bizzi, A., Dell'Acqua, F., Allin, M., Walshe, M., Murray, R., Williams, S.C., Murphy, D.G.M., Catani, M., 2011. Atlasing location, asymmetry and inter-subject variability of white matter tracts in the human brain with MR diffusion tractography. NeuroImage 54, 49–59.

Denk, C., Rauscher, A., 2010. Susceptibility weighted imaging with multiple echoes. J. Magn. Reson. Imaging 31, 185–191.

Denk, C., Hernandez Torres, E., MacKay, A., Rauscher, A., 2011. The influence of white matter fibre orientation on MR signal phase and decay. NMR Biomed. 24, 246–252.

Descoteaux, M., Angelino, E., Fitzgibbons, S., Deriche, R., 2007. Regularized, fast, and robust analytical Q-Ball imaging. Magn. Reson. Med. 58, 497–510.

Duyn, J.H., 2010. Study of brain anatomy with high-field MRI: recent progress. Magn. Reson. Imaging 28, 1210–1215.

Dyrby, T.B., Søgaard, L.V., Parker, G.J., Alexander, D.C., Lind, N.M., Baaré, W.F.C., Hay-Schmidt, A., Eriksen, N., Pakkenberg, B., Paulson, O.B., Jelsing, J., 2007. Validation of *in vitro* probabilistic tractography. NeuroImage 37, 1267–1277.

Ebeling, U., Reulen, H.J., 1988. Neurosurgical topography of the optic radiation in the temporal lobe. Acta Neurochir. (Wien) 92, 29–36.

Felleman, D.J., Van Essen, D.C., 1991. Distributed hierarchical processing in the primate cerebral cortex. Cereb. Cortex 1, 1–47.

Fischl, B., Sereno, M.I., Dale, A.M., 1999. Cortical surface-based analysis. II: inflation, flattening, and a surface-based coordinate system. NeuroImage 9, 195–207.

Fukunaga, M., Li, T.Q., van Gelderen, P., de Zwart, J.A., Shmueli, K., Yao, B., Lee, J., Maric, D., Aronova, M.A., Zhang, G.F., Leapman, R.D., Schenck, J.F., Merkle, H., Duyn, J.H., 2010. Layer-specific variation of iron content in cerebral cortex as a source of MRI contrast. Proc. Natl. Acad. Sci. U. S. A. 107, 3834–3839.

Gati, J.S., Menon, R.S., Ugurbil, K., Rutt, B.K., 1997. Experimental determination of the BOLD field strength dependence in vessels and tissue. Magn. Reson. Med. 38, 296–302.

Geschwind, N., 1965. Disconnexion syndromes in animals and man. I. Brain 88, 237–294.

Gigandet, X., Hagmann, P., Kurant, M., Cammoun, L., Meuli, R., Thiran, J.-P., 2008. Estimating the confidence level of white matter connections obtained with MRI tractography. PLoS One 3, e4006.

Goldman-Rakic, P.S., Selemon, L.D., Schwartz, M.L., 1984. Dual pathways connecting the dorsolateral prefrontal cortex with the hippocampal formation and parahippocampal cortex in the rhesus monkey. Neuroscience 12, 719–743.

Haacke, E.M., Xu, Y.B., Cheng, Y.C.N., Reichenbach, J.R., 2004. Susceptibility weighted imaging (SWI). Magn. Reson. Med. 52, 612–618.

He, X., Yablonskiy, D.A., 2009. Biophysical mechanisms of phase contrast in gradient echo MRI. Proc. Natl. Acad. Sci. U. S. A. 106, 13558–13563.

Heidemann, R.M., Porter, D.A., Anwander, A., Feiweier, T., Heberlein, K., Knösche, T.R., Turner, R., 2010. Diffusion imaging in humans at 7 T using readout-segmented EPI and GRAPPA. Magn. Reson. Med. 64, 9–14.

Jones, D.K., 2003. Determining and visualizing uncertainty in estimates of fiber orientation from diffusion tensor MRI. Magn. Reson. Med. 49, 7–12.

Jones, D.K., Simmons, A., Williams, S.C.R., Horsfield, M.A., 1999. Non-invasive assessment of axonal fiber connectivity in the human brain via diffusion tensor MRI. Magn. Reson. Med. 42, 37–41.

Kitajima, M., Korogi, Y., Takahashi, M., Eto, K., 1996. MR signal intensity of the optic radiation. Am. J. Neuroradiol. 17, 1379–1383.

Koopmans, P.J., Manniesing, R., Niessen, W.J., Viergever, M.A., Barth, M., 2008. MR venography of the human brain using susceptibility weighted imaging at very high field strength. Magn. Reson. Mater. Phys. Biol. Med. 21, 149–158.

Kroon, D.-J., Slump, C.H., 2009. Coherence filtering to enhance the mandibular canal in cone-beam CT data. IEEE-EMBS Benelux Chapter, Enschede, The Netherlands.

Langkammer, C., Krebs, N., Goessler, W., Scheurer, E., Ebner, F., Yen, K., Fazekas, F., Ropele, S., 2010. Quantitative MR imaging of brain iron: a postmortem validation study. Radiology 257, 455–462.

Lawes, I.N.C., Barrick, T.R., Murugam, V., Spierings, N., Evans, D.R., Song, M., Clark, C.A., 2008. Atlas-based segmentation of white matter tracts of the human brain using diffusion tensor tractography and comparison with classical dissection. NeuroImage 39, 62–79.

Lee, J., van Gelderen, P., Kuo, L.-W., Merkle, H., Silva, A.C., Duyn, J.H., 2011. T2*-based fiber orientation mapping. NeuroImage 57, 225–234.

Li, T.Q., van Gelderen, P., Merkle, H., Talagala, L., Koretsky, A.P., Duyn, J., 2006. Extensive heterogeneity in white matter intensity in high-resolution T2*-weighted MRI of the human brain at 7.0 T. NeuroImage 32, 1032–1040.

Li, T.Q., Yao, B., van Gelderen, P., Merkle, H., Dodd, S., Talagala, L., Koretsky, A.P., Duyn, J., 2009. Characterization of T2* heterogeneity in human brain white matter. Magn. Reson. Med. 62, 1652–1657.

Liu, C.L., 2010. Susceptibility tensor imaging. Magn. Reson. Med. 63, 1471–1477.

Liu, T., Spincemaille, P., de Rochefort, L., Kressler, B., Wang, Y., 2009. Calculation of Susceptibility Through Multiple Orientation Sampling (COSMOS): a method for conditioning the inverse problem from measured magnetic field map to susceptibility source image in MRI. Magn. Reson. Med. 61, 196–204.

Locke, S., Yakovlev, P.I., 1965. Transcallosal connections of the cingulum of man. Arch. Neurol. 13, 471–476.

Martino, J., Brogna, C., Robles, S.G., Vergani, F., Duffau, H., 2010. Anatomic dissection of the inferior fronto-occipital fasciculus revisited in the lights of brain stimulation data. Cortex 46, 691–699.

McNab, J.A., Jbabdi, S., Deoni, S.C.L., Douaud, G., Behrens, T.E.J., Miller, K.L., 2009. High resolution diffusion-weighted imaging in fixed human brain using diffusion-weighted steady state free precession. NeuroImage 46, 775–785.

McNab, J.A., Gallichan, D., Miller, K.L., 2010. 3D steady-state diffusion-weighted imaging with Trajectory Using Radially Batched Internal Navigator Echoes (TURBINE). Magn. Reson. Med. 63, 235–242.

Mori, S., Crain, B.J., Chacko, V.P., van Zijl, P.C.M., 1999. Three-dimensional tracking of axonal projections in the brain by magnetic resonance imaging. Ann. Neurol. 45, 265–269.
Mori, N., Miki, Y., Kasahara, S., Maeda, C., Kanagaki, M., Urayama, S., Sawamoto, N., Fukuyama, H., Togashi, K., 2009. Susceptibility-weighted imaging at 3 Tesla delineates the optic radiation. Investig. Radiol. 44, 140–145.
Morris, D.M., Embleton, K.V., Parker, G.J.M., 2008. Probabilistic fibre tracking: differentiation of connections from chance events. NeuroImage 42, 1329–1339.
Nieuwenhuys, R., Voogd, J., van Huijzen, C., 2008. The human central nervous system, 4th ed. Springer-Verlag, Berlin, Heidelberg, New York.
Ogawa, S., Lee, T.M., Kay, A.R., Tank, D.W., 1990. Brain magnetic resonance imaging with contrast dependent on blood oxygenation. Proc. Natl. Acad. Sci. U. S. A. 87, 9868–9872.
Parker, G.J.M., Haroon, H.A., Wheeler-Kingshott, C.A.M., 2003. A framework for a streamline-based Probabilistic Index of Connectivity (PICo) using a structural interpretation of MRI diffusion measurements. Journal of Magnetic Resonance Imaging 18. 242–254.
Passingham, R.E., Stephan, K.E., Kotter, R., 2002. The anatomical basis of functional localization in the cortex. Nature Reviews Neurosience 3, 606–616.
Reichenbach, J.R., Venkatesan, R., Schillinger, D.J., Kido, D.K., Haacke, E.M., 1997. Small vessels in the human brain: MR venography with deoxyhemoglobin as an intrinsic contrast agent. Radiology 204, 272–277.
Roebroeck, A., Galuske, R., Formisano, E., Chiry, O., Bratzke, H., Ronen, I., Kim, D.S., Goebel, R., 2008. High-resolution diffusion tensor imaging and tractography of the human optic chiasm at 9.4 T. NeuroImage 39, 157–168.
Röttger, D., Seib, V., Müller, S., 2011. Distance-based tractography in high angular resolution diffusion MRI. Vis. Comput. 27, 729–738.
Schäfer, A., Wiggins, C.J., Turner, R., 2009. Understanding the orientation dependent T2* contrast of the cingulum in ultra high fields. Proceedings of the 17th Annual Meeting of ISMRM. Honolulu, Hawaii, p. 956.
Schmahmann, J.D., Pandya, D.N., 2007. The complex history of the fronto-occipital fasciculus. J. Hist. Neurosci. Basic Clin. Perspect. 16, 362–377.
Schweser, F., Deistung, A., Lehr, B.W., Reichenbach, J.R., 2011. Quantitative imaging of intrinsic magnetic tissue properties using MRI signal phase: an approach to *in vivo* brain iron metabolism? NeuroImage 54, 2789–2807.
Seunarine, K.K., Alexander, D.C., 2009. Multiple fibers: beyond the diffusion tensor. In: Heidi, J.-B., Timothy, E.J.B. (Eds.), Diffusion MRI. Academic Press, San Diego, pp. 55–72.
Seunarine, K.K., Cook, P.A., Hall, M.G., Embleton, K.V., Parker, G.M.J., Alexander, D.C., 2007. Exploiting peak anisotropy for tracking through complex structures. IEEE ICCV Workshop on MMBIA.
Smith, S.M., Jenkinson, M., Woolrich, M.W., Beckmann, C.F., Behrens, T.E.J., Johansen-Berg, H., Bannister, P.R., De Luca, M., Drobnjak, I., Flitney, D.E., Niazy, R.K., Saunders, J., Vickers, J., Zhang, Y.Y., De Stefano, N., Brady, J.M., Matthews, P.M., 2004. Advances in functional and structural MR image analysis and implementation as FSL. NeuroImage 23, S208–S219.
Tournier, J.D., Mori, S., Leemans, A., 2011. Diffusion tensor imaging and beyond. Magn. Reson. Med. 65, 1532–1556.
Tuch, D.S., 2004. Q-Ball imaging. Magn. Reson. Med. 52, 1358–1372.
Tusa, R.J., Ungerleider, L.G., 1985. The inferior longitudinal fasciculus — a reexamination in humans and monkeys. Ann. Neurol. 18, 583–591.
Tusa, R.J., Ungerleider, L.G., 1988. Fiber pathways of cortical areas mediating smooth pursuit eye-movements in monkeys. Ann. Neurol. 23, 174–183.
van Baarsen, K.M., Porro, G.L., Wittebol-Post, D., 2009. Epilepsy surgery provides new insights in retinotopic organization of optic radiations. A systematic review. Curr. Opin. Ophthalmol. 20, 490–494.
Visser, E., Qin, S., Zwiers, M.P., 2010. EPI distortion correction by constrained nonlinear coregistration improves group fMRI. International Society for Magnetic Resonance in Medicine, Stockholm, p. 3459.
Wedeen, V.J., Wang, R.P., Schmahmann, J.D., Benner, T., Tseng, W.Y.I., Dai, G., Pandya, D.N., Hagmann, P., D'Arceuil, H., de Crespigny, A.J., 2008. Diffusion spectrum magnetic resonance imaging (DSI) tractography of crossing fibers. NeuroImage 41, 1267–1277.
Weickert, J., 1998. Anisotropic Diffusion in Image Processing. B.G. Teubner, Stuttgart.
Weickert, J., Scharr, H., 2002. A scheme for coherence-enhancing diffusion filtering with optimized rotation invariance. J. Vis. Commun. Image Represent. 13, 103–118.
Wiggins, C.J., Gudmundsdottir, V., Le Bihan, D., Lebon, V., Chaumeil, M., 2008. Orientation dependence of white matter T2* contrast at 7 T: a direct demonstration. Proceedings of the 16th Annual Meeting of ISMRM, Toronto, Canada, p. 237.
Woodward, W.R., Coull, B.M., 1984. Localization and organization of geniculocortical and corticofugal fiber tracts within the subcortical white matter. Neuroscience 12, 1089–1099.
Yeterian, E.H., Pandya, D.N., 2010. Fiber pathways and cortical connections of preoccipital areas in rhesus monkeys. J. Comp. Neurol. 518, 3725–3751.
Zwiers, M.P., 2010. Patching cardiac and head motion artefacts in diffusion-weighted images. NeuroImage 53, 565–575.